TITLE: Engineering grain boundary energy with thermal profiles to control grain growth in $SrTiO_3$

AUTHORS: Vivekanand Muralikrishnan[1], Jackson Langhout[2], Daniel P. Delellis[1], Kristy Schepker[2], Amanda R. Krause[1*]

[1]Department of Materials Science and Engineering, Carnegie Mellon University, Pittsburgh, PA 15213
[2]Department of Materials Science and Engineering, University of Florida, Gainesville, FL 32611
[*]Corresponding Author: amandakr@andrew.cmu.edu

JOURNAL: Journal of the American Ceramic Society

Volume: 107

Year: 2024

Pages: 7062-7071

KEYWORDS: grain boundaries, grain growth, heat treatment, strontium titanate

DOI: 10.1111/jace.19982

Abstract

This study investigates the influence of thermal history on grain boundary (GB) energy and the grain growth behavior of $SrTiO_3$ at 1425°C. Two thermal profiles were explored: (1) a single-step sintering at 1425°C for 1hr and (2) a two-step profile with sintering completed at 1425°C for 1hr with an additional 10hr at 1350°C. Electron backscattered diffraction and atomic force microscopy were utilized to measure the grain size and GB energy distributions, respectively, for the samples before and after grain growth at 1425°C for 10hr. The two-step profile exhibits fewer abnormal grains and a slower growth rate at 1425°C than the single-step profile. Additionally, the two-step sample comprises few high-energy GBs and a narrow GB energy distribution, which suggests that it had a lower driving force for subsequent grain growth. The thermal profile was able to sufficiently change the growth rate such that the two-step sample results in a finer grain size than observed for the single-step sample after 10hr at 1425°C despite being exposed to elevated temperatures for almost twice as long. These results suggest that GB energy engineering through thermal profile modification can be used to control the grain growth rate and abnormal grain growth likelihood.

1. Introduction

The phenomenon of abnormal grain growth (AGG), in which a small fraction of grains grows faster than their neighbors, is essential to predict for producing a desirable microstructure with optimum performance. Often, preventing AGG is desirable to create unimodal grain size distributions and, hence, remove any deleterious effects in bulk properties caused by heterogeneous microstructures (1–3). However, initiating and promoting AGG may be a potential energy-efficient and cost-friendly pathway to fabricating single crystals by engineering a single abnormal grain to consume the entire microstructure (4–8). Therefore, significant efforts have focused on controlling AGG in ceramics prepared by powder processing.

Methods to control grain growth rate and AGG in ceramics include controlling the dopant type and concentration (9–17), sintering atmosphere (18–21), heating rates (22), thermal profile (18,22–26), or a combination thereof. In particular, multi-step thermal profiles have been shown to have significant effects on the grain growth rates and AGG behavior in many ceramic systems, including MgO - doped Al_2O_3 (22), $SrTiO_3$ (23,24), $BaTiO_3$ (18) and WC-Co (25). Often, the temperature profile is optimized to achieve densification quickly to minimize the time at high temperatures when grain growth is fast (27,28). However, Kermani et al. (22) demonstrated in MgO-doped Al_2O_3 that the grain growth rate at elevated temperatures after densification could be affected by the thermal history. Specifically, they showed that pre-heating at lower temperatures before final sintering changed the distribution of MgO at the grain boundaries (GBs), which they suggested changed the GB mobility and, thus, the resulting grain growth rate. Their study did not observe abnormally large grains, but others have similarly postulated that the thermal profile can be used to engineer the GB structure to alter the onset of AGG (18,25,26).

GB energy anisotropy is also shown to affect the propensity of AGG (9,16,29–32). Prior studies in ceramics, which include different doped Al_2O_3 systems (30,32) and Ca-doped Y_2O_3 (9,31), have demonstrated that the GBs for abnormal grains have, on average, lower energy than those for small matrix grains. Additionally, in a recent study in Ca-doped Al_2O_3, Conry et al. (32) observed that AGG was prevented in the textured alumina sample compared to the untextured alumina sample due to its unique GB character and energy distribution. Similarly, Handwerker et al. (16) saw no AGG in doped alumina microstructures that showed a narrow distribution of dihedral angles at the triple junctions (observations from 2D micrographs), suggesting a narrow GB energy distribution. These studies indicate that methods to control GB energy distribution can be used to control AGG.

This study investigates whether the thermal profile can control the GB energy distributions to significantly alter AGG in strontium titanate ($SrTiO_3$). $SrTiO_3$ is chosen as a material for this study because of its well-studied grain growth behavior (23,24,33) and previous studies show that its GB energy distribution depends on temperature (29,34). Therefore, a two-step heat treatment was investigated to observe if the GB energy could be altered to change subsequent grain growth behavior. To avoid variations in densification, all samples were sintered under the same conditions (1425°C for 1 hr in oxidizing conditions) to reach 98% of theoretical density (5.12 g/cm^3). One type of sample was subsequently heat treated at 1350°C for 10 hrs before the grain growth study at 1425°C. The step temperature of 1350°C was chosen because previous studies at this temperature showed no AGG (23,33) and a significant difference in GB energy distribution compared to those heat treated at higher temperatures (29). This two-step sample's subsequent grain growth at 1425°C was compared to samples only exposed to a single-step thermal profile at 1425°C. Grain growth was studied at 1425°C at which AGG is known to occur on a reasonable timescale (23,33). Samples exposed to the two-step heat treatment exhibited a reduced grain growth rate and a smaller fraction of abnormal grains at 1425°C after 10 hrs. The relationship with grain growth and the observed GB energy distributions were evaluated and discussed below. This study highlights the significance of utilizing heat treatments to engineer the microstructure's GB energy, which can be a potential pathway for controlling AGG.

2. Experimental Methods

2.1. $SrTiO_3$ Sample preparation

$SrTiO_3$ powders were synthesized using the solid-state synthesis technique as described in Ref (35) with high purity strontium carbonate (99.9% pure, Sigma Aldrich) and titanium dioxide (99.9% pure, Sigma Aldrich) as precursor materials. Briefly, the process involved mixing the precursor materials at the desired stoichiometric cation ratio in 2-propanol with

zirconia milling media for 24 hr in a rolling mill. After mixing, the solution was dried and then calcined at 925°C for 12 hr in a muffle furnace, in air. The Sr:Ti molar ratio of the synthesized powders used in this study is approximately 1.04, as determined by the x-ray diffraction (XRD) in Section 2.2. The synthesized powders were uniaxially pressed in a 25 mm diameter die and then cold isostatically pressed (50 MPa) to form the green body.

Pellets underwent pressure-less sintering at 1425°C for 1 hr in an oxidizing environment. The as-sintered density was measured using the Archimedes method with a Mettler Toledo XSR balance and density kit. All samples for the grain growth study were cut from the same as-sintered monolith.

Samples were subjected to different heating profiles to create different initial microstructural states. The as-sintered samples (exposed to 1425°C for 1 hr) will be referred to as the single-step samples throughout this document. The two-step samples refer to those that, after sintering at 1425°C for 1 hr, underwent an additional heat treatment at 1350°C for 10 hr. The single-step and two-step samples were then subjected to a heat treatment at 1425°C for 10 hr to evaluate the effect of the heat treatments on subsequent grain growth behavior. Additional heat treatments that are evaluated in this study are provided in the supplemental information.

Sintering and heat treatments were completed with a heating rate of 100°C/hr in a Pt crucible using a tube furnace under flowing oxygen at ~0.25 L/min. Between and after all sintering and heat treatments, samples were furnace cooled to room temperature. The heat treatment time reported is the isothermal dwell time and does not include the exposure during heating and cooling. During the sintering and heat treatment process, the samples were covered using a Sr-rich $SrTiO_3$ powder to prevent the volatilization of SrO from the surface of the sample (36).

2.2. Powder characterization by X-ray diffraction (XRD)

To determine the phases and Sr:Ti molar ratio in the as-synthesized powders, XRD was performed on a Panalytical X'Pert Pro diffractometer equipped with a copper x-ray tube and an X'Celerator RTMS detector. The sample was packed into a backfill sample holder. The sample scan was collected over a 2θ range of 10-80°, with a step size of 0.016° per step and counting time of 17 sec/step. The resulting diffractogram was phase matched using the 2021 edition of the Jade Pro software package (37) and the 2022 PDF-4+ database (38). The software was used to search and phase fit to the collected data restricting matches to only the Sr, Ti and O elements with no additional search restrictions. Jade was allowed to calculate a profile fit and determine abundances of the phases determined to be present. No additional refinement calculations were necessary because all peaks were matched.

2.3. Microstructure characterization

For electron microscopy (EM) characterization, the heat-treated samples were mounted in epoxy and polished down to 250 nm finish using diamond and silica suspensions by standard metallographic techniques. The polished samples were thermally etched and then coated with 0.5 nm Ir. The thermal etching conditions for EM characterization were 1350°C for 40 min for the two-step samples before growth at 1425°C, and 1425°C for 20 min for all other samples.

Secondary electron images of the microstructures were acquired using a Tescan MIRA3 scanning electron microscope (SEM). Electron backscattered diffraction (EBSD) maps of the microstructures were obtained at 30 kV accelerating voltage using the EDAX Hikari Super EBSD camera on the FEI Scios Dual Beam System. Matlab's MTEX package (39) was used to extract the grain size and area from the EBSD maps. The grain size reported here is the equivalent spherical diameter. For each sample, EBSD maps were collected in 9 different areas such that at least 5,000 grains and 30,000 grains were collected in the samples that exhibited normal grain growth (NGG) and AGG, respectively. AGG was first assessed by visually scanning over the sample for grains significantly larger than their neighbors. Over 30,000

grains were sampled from the microstructures with AGG for better statistics. The field of view was chosen to capture both the abnormal and matrix grains simultaneously. EBSD maps were collected with a step size of 0.2 μm for samples exhibiting NGG and 0.3 μm or 0.4 μm for samples exhibiting AGG.

2.3. Relative GB energy measurement

Atomic Force Microscopy (AFM) was utilized to measure the dihedral angles formed by the GB thermal grooves and thereby determine the relative GB energy as described in previous studies (9,29–32,40–42). The samples for the relative GB energy determination from AFM measurements were thermally etched at 1425°C for 40 min in an oxidizing atmosphere. This thermal etching condition used for AFM measurements is different from the thermal etching condition used for the EM measurements stated above to optimize the groove width (>250 nm, as determined by (40–42)). The groove geometry was measured using a Bruker Icon Dimension IV AFM in contact mode with a pyramidal silicon nitride tip (Nanoworld PNP-TR) which had a cone angle of 35º, a nominal tip radius of less than 10 nm, and a force constant of 0.32 N/m. AFM maps for each sample were collected with a step size of 10 nm and at random locations of the sample.

To determine the dihedral angles, the geometries of the thermal grooves from the AFM maps were extracted by drawing boxes of variable width perpendicular to the GB using the step measuring tool in the Nanoscope software. Figure 1 provides an example of the GB groove collected from the AFM map. From the averaged line profile of each GB thermal groove, the depth (d_L, d_R) and width (W_L, W_R) for the left and right side of each groove were extracted. The relative GB energy ($^{\gamma_{gb}}/_{\gamma_s}$) was calculated using the method proposed by Mullins (43) with

$$\varphi_s = 180 - 2\tan^{-1}\left(\frac{mean(d_L, d_R)}{2(W_L + W_R)} * m\right) \quad (1)$$

$$\frac{\gamma_{gb}}{\gamma_s} = 2\cos\frac{\varphi_s}{2} \quad (2)$$

where φ_s is the dihedral angle, γ_{gb} is the GB energy, γ_s is the surface energy, and m is the correction factor for the groove geometry which is taken to be 4.73, as reported by Mullins (43).

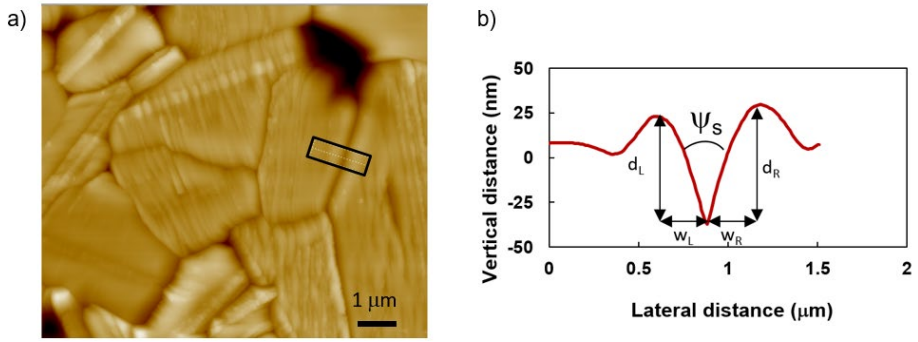

Figure 1. (a) Example AFM map of a region of interest collected at 10 nm lateral resolution. (b) Average line profile of the GB thermal groove collected from the area outlined in black in (a).

It is important to note that there are a number of approximations that goes into the relative GB energy calculation (Eq. 2). First, it is assumed that the two surface energies are the same. Additionally, it is assumed that the GB is normal to the surface and that the torque terms are negligible. Despite these assumptions, previous studies have shown that the relative GB energy distributions are meaningful quantities when sufficient number of boundaries are measured (9,29–32,40,41). Hence, for the relative GB energy analysis, 148 and 186 GBs were sampled for the single-step sample and two-step sample, respectively, before growth at 1425°C for 10 hr. The error bar associated with the calculated relative GB energy value was calculated using basic propagation of error rules in Eq. (2) by considering the uncertainty in AFM tip position to be the smallest increment (i.e., step size) divided by 2 (44).

3. Results

3.1. Composition and Density

XRD of the as-synthesized powder in Fig. 2 shows the presence of $SrTiO_3$ and $Sr_3Ti_2O_7$ phases, indicating the as-synthesized powder has a Sr:Ti molar ratio greater than 1 based on the SrO – TiO_2 phase diagram (45). Profile fitting of the XRD pattern revealed the phase fraction to be 90 wt.% $SrTiO_3$ and 10 wt.% $Sr_3Ti_2O_7$, which is in accord with a Sr:Ti molar ratio of 1.04. Information about how the $Sr_3Ti_2O_7$ phase was characterized by Raman Spectroscopy is provided in the supplemental information section S1.

The relative density of the as-sintered samples measured using the Archimedes method is 98% of the theoretical density (5.12 g/cm^3).

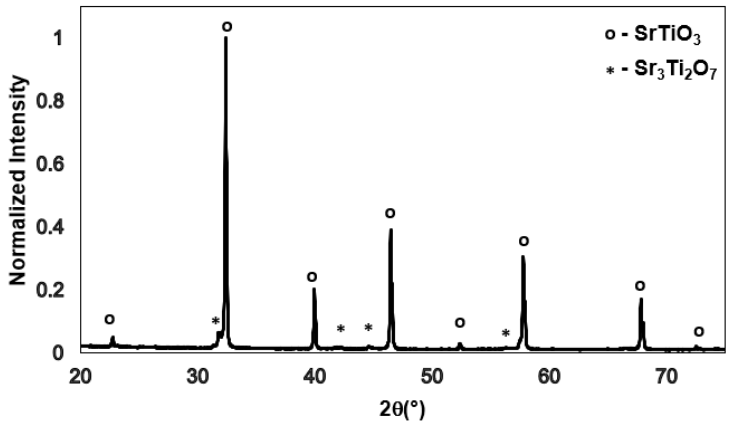

Figure 2. XRD plot of the as-synthesized $SrTiO_3$ powders.

3.2. Grain growth behavior comparison at 1425°C

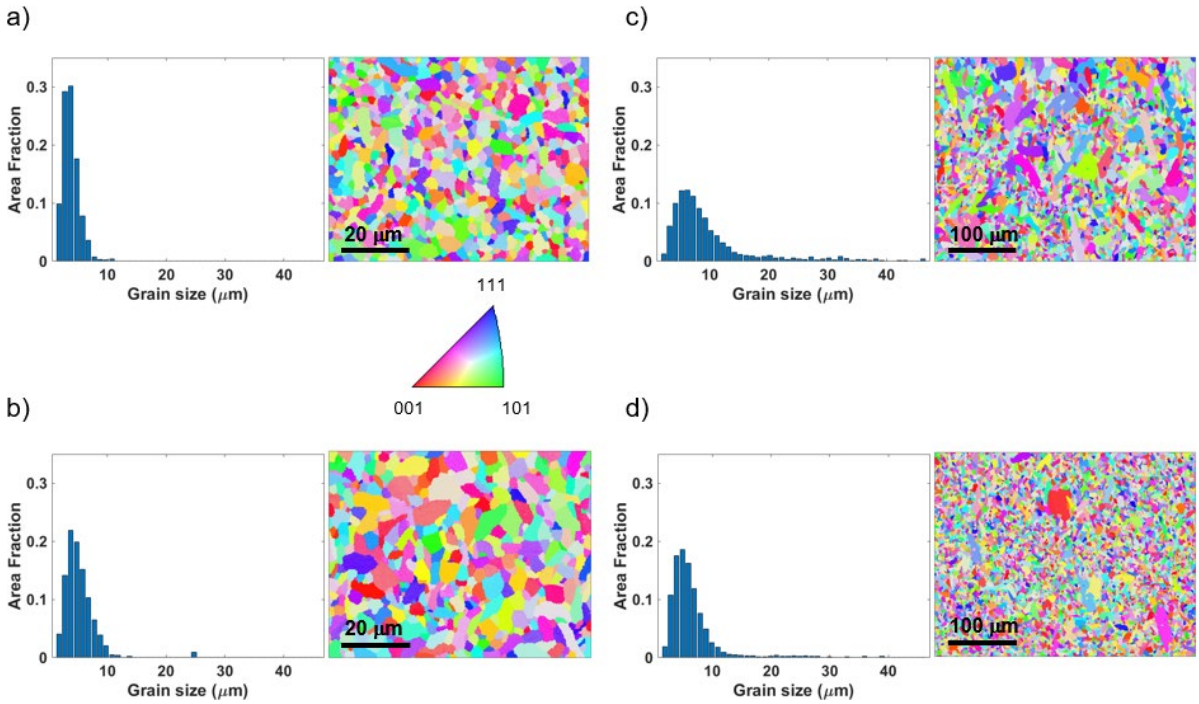

Figure 3. The grain size distributions and representative EBSD microstructure maps for (a) the single-step sample (as-sintered state), (b) two-step sample, (c) single-step sample after heat treatment at 1425°C for 10 hr and (d) two-step sample after heat treatment at 1425°C for 10 hr. The EBSD maps are colored based on inverse pole figure (IPF) key with respect to the image normal direction. Note that the EBSD maps for (a-b) are collected at a different scale than (c-d).

Table 1. Average grain size and abnormal grain area fraction for the different samples.

Sample	Average grain size (μm)	Abnormal grain area fraction (%)
Single-Step	2.3 μm	-
Two-Step	2.9 μm	-
Single-Step after heat treatment at 1425°C for 10 hrs	4.6 μm	13%
Two-Step after heat treatment at 1425°C for 10 hrs	3.6 μm	4%

The results here report the differences in the grain growth evolution of the two initial microstructural states (single-step and two-step sample) at 1425°C for 10 hr. Figures 3a and 3b show the initial grain size distributions and EBSD maps of the single-step and two-step samples, respectively. The average grain size increases from 2.3 μm to 2.9 μm after the heat treatment at 1350°C for 10 hr (Table 1). Additionally, both the initial microstructural states exhibit unimodal grain size distributions, suggesting NGG at 1350°C (for 10 hr) for $SrTiO_3$ samples sintered at 1425°C for 1 hr.

Figures 3c and 3d show the grain size distribution and representative EBSD maps of the single-step and two-step samples, respectively, after heat treatment at 1425°C for 10 hr. After heat treatment at 1425°C for 10 hr, both the single-step and two-step samples show large grains surrounded by many small grains and exhibit a long tail in the grain size distribution, indicating AGG for long exposures at 1425ºC. The representative EBSD maps (Figs. 3c and 3d) qualitatively show, within the same area microstructure map, a larger abnormal grain area fraction formed after growth for the single-step sample compared to the two-step sample. This qualitative observation is validated quantitatively by calculating the abnormal grain area fraction (Table 1). The minimum threshold for abnormal grain size is determined by plotting the normal probability plots for grain size distributions and identifying the grain size at which the grain size distribution deviates positively from log normality (46), as described in the supplemental information section S2. The abnormal grain area fraction after growth at 1425°C for 10 hr for the single-step sample (13%) was greater than that for the two-step sample (4%) based on a threshold of 15 μm and 14 μm threshold, respectively.

Notably, the sample that experienced the longest time at elevated temperature (1350°C for 10 hr + 1425°C for 10 hr) had a smaller average grain size (3.6 μm) than the sample only exposed to 1425°C for 10 hr (4.6 μm). The final small grain size is due to the slower growth rate of the matrix grains for the two-step sample compared to the single-step sample during the same heat treatment exposure of 1425°C for 10 hr.

In conclusion, the two-step sample has a larger initial average grain size, slower growth rate for matrix grains, and a smaller fraction of abnormal grains formed after growth at 1425°C for 10 hr than observed for the single-step sample.

3.2. GB energy distribution comparison between the two initial microstructural states

The relative GB energy cumulative distribution for the two initial microstructural states is compared in Fig. 4. The relative GB energy distributions for the two different initial

microstructural states are statistically different via a two sample Kolmogorov-Smirnov test (p value = 0.03). Furthermore, qualitative observations from the relative GB energy distributions show that the relative GB energy distribution of the two-step sample is narrower and shifted towards lower energy when compared to the single-step sample. This indicates that the two-step sample has fewer high energy GBs compared to the single-step sample. Additionally, this result also suggests that the grain growth at 1350°C for 10 hr preferentially removes high energy GBs, which is expected for grain growth as shown in previous studies (32,47,48).

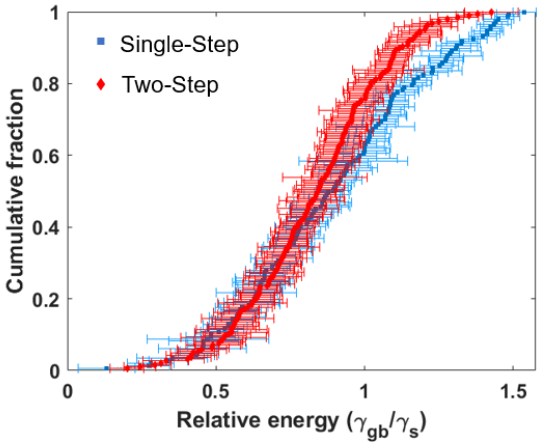

Figure 4. Cumulative distribution of Relative GB energy for the single-step and two-step sample.

4. Discussion

The motivation of the work is to investigate the effect of thermal history on the initiation of AGG in $SrTiO_3$. To that end, the grain size distributions (Fig. 3) and fraction of abnormal grains (Table 1) were evaluated at 1425ºC for 10 hr for the samples with different initial heating profiles. Additionally, the relative GB energy distribution (Fig. 4) for the different initial microstructural states were collected to correlate to the AGG behavior. In summary this study found that, in comparison to the single-step sample (as sintered – 1425°C for 1hr), the two-step sample (as-sintered + heat treated at 1350°C for 10 hr) has

1) a slower growth rate for matrix grains at 1425ºC,

2) a smaller fraction of abnormal grains formed after grain growth at 1425ºC for 10 hr, and

3) fewer high-energy GBs and a narrower GB energy distribution prior to growth at 1425ºC.

Based on this summary of findings, the subsequent subsections will focus on discussing the potential reasons for why the thermal history modification affects the AGG behavior and growth rate of matrix grains.

4.1. The influence of the GB energy and grain size on the AGG behavior

The global driving force for grain growth is the reduction of the total free energy of the system, where free energy is the product of the GB energy (γ) and its area (A). The GB energy is a function of its macroscopic character, atomic structure, and chemistry. In the absence of any stored energy, the total free energy of the system during grain growth is reduced with time through a combination of GB area reduction (γdA) and GB energy reduction ($Ad\gamma$). Notably, Xu et al. (47) recently showed experimental evidence in Ni that free energy dissipation during grain growth occurs through both GB area reduction and GB energy reduction, in which low energy GBs replace high energy GBs. The two-step sample, which underwent grain growth at 1350°C for 10 hr after sintering, showed a decrease in total GB area (evident from the increase in grain size from 2.3 μm to 2.9 μm) and a shift in GB energy distribution to fewer high energy GBs, which may reflect a similar GB replacement mechanism.

The narrow relative GB energy distribution may explain why the two-step sample (as-sintered + heat treated at 1350°C for 10 hr) has a smaller fraction of abnormal grains formed after grain growth at 1425°C for 10 hr than the single-step sample (as-sintered). As discussed in the introduction, broader GB energy distributions have been correlated with the initiation and growth of abnormal grains. Furthermore, previous experiments have shown that abnormal grains have, on average, lower GB energy than neighboring grains (9,30–32). Mesoscale grain growth simulations have shown that one possible way to cause AGG is by assigning certain GBs lower energy than their neighbors, giving them a growth advantage (49,50). Hence, one

interpretation provided by Conry et al. (32) was that a narrower GB energy distribution has a lower incentive for AGG because of a smaller difference in energy between neighboring boundaries. In agreement with that hypothesis, the two-step sample, which has a narrower distribution in GB energy, observes a smaller abnormal grain area fraction after growth at 1425°C for 10 hr.

In addition to the larger distribution, the as-sintered microstructure state contains boundaries with a higher energy than found in the two-step sample, which may affect the AGG behavior. High-energy GBs have been shown to be associated as the preferential sites for initiating AGG in a study by Bojarski et al. (51). They hypothesized that these high-energy GBs are preferred nucleation sites for GB complexion transitions, in which a GB undergoes a 2D phase-like transformation to a lower energy structure. Others have previously hypothesized that such GB complexion transitions can lead to AGG (9–15). Therefore, the presence of higher energy GBs in the single-step sample compared to the two-step microstructure may increase the probability of GB complexion transitions, resulting in greater AGG.

AGG in $SrTiO_3$ has also previously been hypothesized to result from solute/space charge drag associated with variations in the Sr:Ti ratio at the GBs (52) or an interface controlled migration mechanism resulting from $SrTiO_3$ GBs being atomically faceted (53). According to both of these mechanisms, the velocity of the GB is a non-linear function of driving force, and the boundary must overcome a critical driving force to move. AGG would occur if only a small fraction of boundaries overcome the critical driving force. The local driving force for grain growth has been suggested to be the energy difference between neighboring GBs, where low energy GBs replace neighboring high-energy GBs as grain growth proceeds (47,48). Therefore, AGG may be suppressed or delayed in the two-step sample because it has a lower probability of overcoming the critical driving force due to its narrower GB energy distribution relative to the single-step sample.

In addition to differences in the GB energy distribution, the two heat treatment profiles result in different grain sizes that can affect the number of potential initiation sites for AGG. Given that the two-step sample has a larger average grain size and, thus, fewer grains per unit area, it may have fewer initiation events for AGG. However, the single-step sample reaches a similar average grain size and grain size distribution as the two-step sample during growth at 1425°C for 2 hr, as shown in the supplemental information section S3. Additionally, no AGG is observed at that stage, indicating that the grain size differences between the initial microstructural states had a negligible effect on the differences in subsequent AGG observed after heat treatment at 1425°C for 10 hr.

It is important to note that the grain size distribution in Fig. 3b may suggest that AGG initiated at 1350°C after 10 hr, which can influence its subsequent AGG behavior. Abnormal grains observed after 10 hr at 1425°C in the two-step sample may have been those that initiated at 1350°C. However, such growth does not explain why the two-step sample results in smaller and fewer abnormal grains than the single-step sample after further heating for 10 hr at 1425°C.

In summary, the thermal profile that led to few high-energy GBs and a narrow GB energy distribution experiences less AGG at 1425°C. This suggests that engineering GB energy through heat treatments can potentially prevent AGG and should be explored in other systems.

4.2. The influence of the GB energy and grain size on the matrix grains growth rate

An interesting observation from this study was that the differences in growth rates for matrix grains allowed for the sample that experienced longer time at elevated temperatures (1350°C for 10 hr + 1425°C for 10 hr) to have a smaller average grain size compared to the sample which experienced shorter times at elevated temperatures (1425°C for 10 hr). Similar to the AGG behavior, the differences in growth rates could reflect their unique GB energy distributions. If the local driving force is the energy difference between neighboring GBs

(47,48), the two-step sample, which has fewer high-energy GBs, would have a smaller driving force for grain growth, resulting in a slower growth rate.

Alternatively, it is generally accepted that the larger the average grain size, the smaller the driving force for grain growth. Therefore, the two-step sample, which has a larger average grain size compared to the single-step sample, could also lead to the smaller driving force. However, it is important to note that even though single-step sample has a smaller initial average grain size, it attains a similar average grain size (3 μm, Fig. S3) to the two-step sample (2.9 μm) after grain growth at 1425°C for 2 hr and then continues to grow at a faster rate. If the grain size was the sole governing driving force for growth, then a similar grain growth rate would be observed at 1425°C between samples, and the as-sintered sample would have a smaller final grain size. Therefore, the faster growth rate suggests that the difference in GB energy distributions may influence the driving force and, thus, the growth rate. However, GB mobility is another important factor in dictating the grain growth rate. Since GB mobility is difficult to measure experimentally, the role of GB mobility cannot be determined and is beyond the scope of the current study.

Overall, the thermal profile could be modified to produce a microstructure that comprises fewer high-energy GBs and, thus, a potentially lower driving force for grain growth, resulting in a slower growth rate at 1425°C. By lowering the driving force, $SrTiO_3$ samples had a finer final average grain size even when exposed to long times at elevated temperatures, highlighting again the potential of GB energy engineering through heat treatments to control grain growth rate.

4.3. Other effects on grain growth behavior

$SrTiO_3$, due its cubic crystal structure, is expected to have equiaxed grains. However, the microstructures observed in Fig. 3 show elongated grains, which is not typically observed in $SrTiO_3$ microstructures (23,33,54). The XRD in Fig. 2 shows that the synthesized $SrTiO_3$

powders have both $SrTiO_3$ and $Sr_3Ti_2O_7$ phases. The Ruddlesden-Popper ($Sr_3Ti_2O_7$) phases are tetragonal and similar to the perovskite lattice of $SrTiO_3$ but with excess SrO layers between the traditional cubic unit cells (55). With excess SrO in the system, such SrO layers can be introduced as stacking faults into the perovskite lattice creating Ruddlesden-Popper like phases. Hence, the microstructures observed here are likely elongated due to the influence of Ruddlesden-Popper stacking faults (56).

Figure 5 shows representative SEM micrographs of the single-step sample after heat treatment at 1425°C for 10 hr and shows evidence of such Ruddlesden-Popper faults, which are indicated by the white arrows. These faults have been previously identified in Sr-rich $SrTiO_3$ microstructures by transmission electron microscopy analysis (56). These faults are randomly distributed and are found in both the small matrix grains (Fig. 5a) and the large abnormal grains (Fig. 5b). This observation suggests that the distribution of Ruddlesden-Popper stacking faults is not correlated with the AGG behavior. Additionally, Raman spectroscopy analysis (as described in the supplementary information Section S1) showed that the Ruddlesden-Popper ($Sr_3Ti_2O_7$) phase peaks were present throughout for both the initial microstructural state samples. All tested samples showed a similar mean relative intensity for the $Sr_3Ti_2O_7$ peaks, supporting that the Ruddlesden-Popper phases do not cause the differences in the grain growth behavior for the two initial microstructural states.

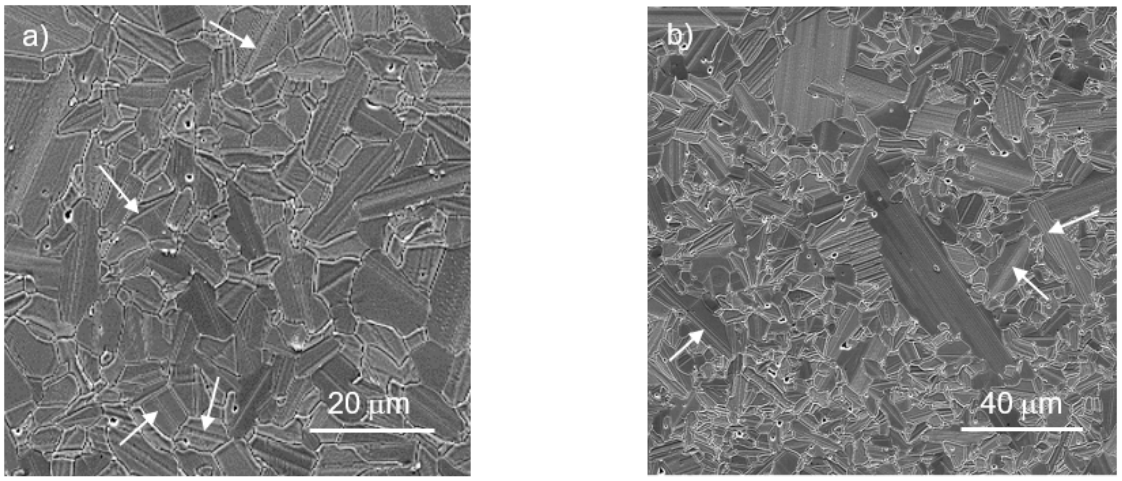

Figure 5. SEM image of (a) matrix grains and (b) abnormal grains in the single-step-sample after heat treatment at 1425°C for 10 hr. The white arrows indicate the suspected Ruddlesden-Popper faults. Note that the images have a different scale.

In this study, the $SrTiO_3$ (Sr:Ti ~ 1.04) microstructure does not show anti-thermal grain growth, in which the growth rate decreases with increase in temperature. Previously, Hoffmann and colleagues observed that $SrTiO_3$ samples with a Sr:Ti ratio of 0.996 (23,33,54), which were sintered under the same conditions as this study, exhibited a slower grain growth rate as the temperature increased from 1350°C to 1425°C. Here, typical Arrhenius behavior is seen in the temperature range of 1350°C to 1425°C; the average grain size observed in this study after heat treatment of 1350°C for 10 hr is 2.9 μm, which is smaller than the average matrix grain size of 4.6 μm for the 1425°C for 10 hr sample. Other studies in $SrTiO_3$ have shown that the non-Arrhenius and Arrhenius temperature regimes depend on the sintering temperature (thermal history), Sr:Ti molar ratios and other impurities (24,57). Specifically, it was proposed by Amaral et al. (58) that the Sr:Ti molar ratio can prominently affect grain growth and densification due to its influence on structure and species diffusivity. Therefore, the lack of non-Arrhenius behavior observed at the temperatures in this study may be caused by the Sr:Ti molar ratio and the presence of the Ruddlesden-Popper stacking faults or the thermal history.

5. Conclusion

This study investigated how thermal history influences the AGG behavior in $SrTiO_3$ by comparing the growth behavior at 1425°C in an as-sintered microstructure (single-step) to one that underwent an additional heat treatment at 1350°C for 10 hr after sintering (two-step). The grain size distributions and the relative GB energy distributions (measured by thermal groove measurements) were evaluated. The analysis revealed that the growth rate and the fraction of abnormal grains increases in samples with more high-energy GBs and a broader GB energy distribution. Additionally, the microstructure that underwent the two-step thermal profile and, thus, experienced a longer time at elevated temperatures has a smaller average grain size and a smaller fraction of abnormal grains after 1425°C for 10 hr than the single-step heat treated microstructure. These results suggest that the initiation and growth of abnormal grains can be controlled by engineering the GB energy through modifying the thermal history. This approach can be easily applied with existing processing setups and is a promising method for microstructural engineering with implications for improving the material's performance. Future studies should explore whether similar thermal methods to those proposed here can prevent AGG and control growth rate in different material systems.

Acknowledgements

The authors acknowledge use of the Materials Characterization Facility at Carnegie Mellon University supported by grant MCF-677785. This work was performed, in part, at the Nanoscale Fabrication and Characterization Facility (a laboratory of the Gertrude E. and John M. Petersen Institute of NanoScience and Engineering) at the University of Pittsburgh and the Research Service Centers of the Herbert Wertheim College of Engineering at the University of Florida. Research was supported by grant no. 2143572 funded by the U.S. National Science Foundation.

Conflict of interest

The authors declare no conflict of interest.

Authors Contributions

VM (Leader) – Conceptualization, Design, Experimentation, Analysis and Writing – Original Draft, JL (Contributor) – Experimentation and Analysis, DPD (Contributor) – Experimentation and Writing, KS (Contributor) – Experimentation, Analysis and Writing, ARK (Advisor) – Conceptualization, Supervision, Writing – Review and Editing.

References

1. Furnish TA, Bufford DC, Ren F, Mehta A, Hattar K, Boyce BL. Evidence that abnormal grain growth precedes fatigue crack initiation in nanocrystalline Ni-Fe. Scr Mater. 2018 Jan;143:15–9.

2. Averback RS, Höfler HJ, Hahn H, Logas JC. Sintering and grain growth in nanocrystalline ceramics. Nanostructured Mater. 1992 Mar;1(2):173–8.

3. Tan Y, Zhang J, Wu Y, Wang C, Koval V, Shi B, et al. Unfolding grain size effects in barium titanate ferroelectric ceramics. Sci Rep. 2015 May 7;5(1):9953.

4. Le PG, Tran HT, Lee JS, Fisher JG, Kim HP, Jo W, et al. Growth of single crystals in the (Na1/2Bi1/2)TiO3–(Sr1–xCax)TiO3 system by solid state crystal growth. J Adv Ceram. 2021 Oct;10(5):973–90.

5. Jiang M, Han S, Zhang J, Song J, Hao C, Deng M, et al. Large-scale grain growth in the solid-state process: From “Abnormal” to “Normal.” J Cryst Growth. 2018 Feb;483:258–64.

6. Kang SJL, Park JH, Ko SY, Lee HY. Solid-State Conversion of Single Crystals: The Principle and the State-of-the-Art. Green DJ, editor. J Am Ceram Soc. 2015 Feb;98(2):347–60.

7. Bordia RK, Kang SL, Olevsky EA. Current understanding and future research directions at the onset of the next century of sintering science and technology. J Am Ceram Soc. 2017 Jun;100(6):2314–52.

8. Scott C, Kaliszewski M, Greskovich C, Levinson L. Conversion of Polycrystalline Al_2O_3 into Single-Crystal Sapphire by Abnormal Grain Growth. J Am Ceram Soc. 2002 May;85(5):1275–80.

9. Bojarski SA, Ma S, Lenthe W, Harmer MP, Rohrer GS. Changes in the Grain Boundary Character and Energy Distributions Resulting from a Complexion Transition in Ca-Doped Yttria. Metall Mater Trans A. 2012 Oct;43(10):3532–8.

10. Dillon SJ, Tang M, Carter WC, Harmer MP. Complexion: A new concept for kinetic engineering in materials science. Acta Mater. 2007 Oct;55(18):6208–18.

11. Dillon SJ, Harmer MP. Relating Grain Boundary Complexion to Grain Boundary Kinetics II: Silica-Doped Alumina. J Am Ceram Soc. 2008 Jul;91(7):2314–20.

12. Dillon SJ, Harmer MP. Relating Grain-Boundary Complexion to Grain-Boundary Kinetics I: Calcia-Doped Alumina. J Am Ceram Soc. 2008 Jul;91(7):2304–13.

13. Dillon S, Harmer M. Multiple grain boundary transitions in ceramics: A case study of alumina. Acta Mater. 2007 Sep;55(15):5247–54.

14. Marvel CJ, Krause AR, Harmer MP. Effect of Eu-doping and grain boundary plane on complexion transitions in $MgAl_2O_4$. J Am Ceram Soc. 2021 Aug;104(8):4203–13.

15. Ma S. Exploring the role of grain boundary complexions in the sintering of yttria ceramics [Ph.D. Dissertation]. Lehigh University; 2010.

16. Handwerker CA, Morris PA, Coble RL. Effects of Chemical Inhomogeneities on Grain Growth and Microstructure in Al $_2$ O $_3$. J Am Ceram Soc. 1989 Jan;72(1):130–6.

17. Berry KA, Harmer MP. Effect of MgO Solute on Microstructure Development in Al $_2$ O $_3$. J Am Ceram Soc. 1986 Feb;69(2):143–9.

18. Jung Y, Choi S, Kang SL. Grain-Growth Behavior during Stepwise Sintering of Barium Titanate in Hydrogen Gas and Air. J Am Ceram Soc. 2003 Dec;86(12):2228–30.

19. Lee BK, Chung SY, Kang SJL. Grain boundary faceting and abnormal grain growth in BaTiO3. Acta Mater. 2000 Apr;48(7):1575–80.

20. Jung Y, Choi S, Kang S. Effect of oxygen partial pressure on grain boundary structure and grain growth behavior in BaTiO3. Acta Mater. 2006 Jun;54(10):2849–55.

21. Fisher JG, Kang SJL. Microstructural changes in (K0.5Na0.5)NbO3 ceramics sintered in various atmospheres. J Eur Ceram Soc. 2009 Sep;29(12):2581–8.

22. Kermani M, Wu J, Liu Z, Zuo F, Lin H, Hu C, et al. Impact of sintering thermal history on MgO-doped alumina: Reduction of grain growth constant through high heating rates. J Am Ceram Soc. 2024 Jan;107(1):132–43.

23. Rheinheimer W, Hoffmann MJ. Non-Arrhenius behavior of grain growth in strontium titanate: New evidence for a structural transition of grain boundaries. Scr Mater. 2015 May;101:68–71.

24. Bäurer M, Weygand D, Gumbsch P, Hoffmann MJ. Grain growth anomaly in strontium titanate. Scr Mater. 2009 Sep;61(6):584–7.

25. Yang DY, Kang SJL. Suppression of abnormal grain growth in WC–Co via pre-sintering treatment. Int J Refract Met Hard Mater. 2009 Jan;27(1):90–4.

26. Schumacher O, Marvel CJ, Kelly MN, Cantwell PR, Vinci RP, Rickman JM, et al. Complexion time-temperature-transformation (TTT) diagrams: Opportunities and challenges. Curr Opin Solid State Mater Sci. 2016 Oct;20(5):316–23.

27. Chen IW, Wang XH. Sintering dense nanocrystalline ceramics without final-stage grain growth. Nature. 2000 Mar;404(6774):168–71.

28. Lóh NJ, Simão L, Faller CA, De Noni A, Montedo ORK. A review of two-step sintering for ceramics. Ceram Int. 2016 Aug;42(11):12556–72.

29. Kelly MN, Rheinheimer W, Hoffmann MJ, Rohrer GS. Anti-thermal grain growth in SrTiO3: Coupled reduction of the grain boundary energy and grain growth rate constant. Acta Mater. 2018 May;149:11–8.

30. Dillon SJ, Harmer MP, Rohrer GS. The Relative Energies of Normally and Abnormally Growing Grain Boundaries in Alumina Displaying Different Complexions. J Am Ceram Soc [Internet]. 2010 Mar [cited 2023 Jun 13]; Available from: https://onlinelibrary.wiley.com/doi/10.1111/j.1551-2916.2010.03642.x

31. Bojarski SA, Knighting J, Ma SL, Lenthe W, Harmer MP, Rohrer GS. The Relationship between Grain Boundary Energy, Grain Boundary Complexion Transitions, and Grain Size in Ca-Doped Yttria. Mater Sci Forum. 2013 Mar;753:87–92.

32. Conry B, Kole M, Burnett WR, Harley JB, Tonks MR, Kesler MS, et al. The evolution of grain boundary energy in textured and untextured Ca-doped alumina during grain growth. J Am Ceram Soc. 2023 Aug 28;jace.19367.

33. Rheinheimer W, Hoffmann MJ. Grain growth transitions of perovskite ceramics and their relationship to abnormal grain growth and bimodal microstructures. J Mater Sci. 2016 Feb;51(4):1756–65.

34. Rheinheimer W, Bäurer M, Chien H, Rohrer GS, Handwerker CA, Blendell JE, et al. The equilibrium crystal shape of strontium titanate and its relationship to the grain boundary plane distribution. Acta Mater. 2015 Jan;82:32–40.

35. Bäurer M, Kungl H, Hoffmann MJ. Influence of Sr/Ti Stoichiometry on the Densification Behavior of Strontium Titanate. J Am Ceram Soc. 2009 Mar;92(3):601–6.

36. Zhu Y, Salvador PA, Rohrer GS. Controlling the termination and photochemical reactivity of the $SrTiO_3$ (110) surface. Phys Chem Chem Phys. 2017;19(11):7910–8.

37. JADE Pro. Livermore, CA, USA: MDI Materials Data; 2021.

38. Gates-Rector S, Blanton T. The Powder Diffraction File: a quality materials characterization database. Powder Diffr. 2019 Dec;34(4):352–60.

39. Bachmann F, Hielscher R, Schaeben H. Grain detection from 2d and 3d EBSD data—Specification of the MTEX algorithm. Ultramicroscopy. 2011 Dec;111(12):1720–33.

40. Syed K, Motley NB, Bowman WJ. Heterointerface and grain boundary energies, and their influence on microstructure in multiphase ceramics. Acta Mater. 2022 Apr;227:117685.

41. Saylor DM, Rohrer GS. Measuring the Influence of Grain-Boundary Misorientation on Thermal Groove Geometry in Ceramic Polycrystals. J Am Ceram Soc. 1999 Jun;82(6):1529–36.

42. Dillon SJ, Harmer MP, Rohrer GS. Influence of interface energies on solute partitioning mechanisms in doped aluminas. Acta Mater. 2010 Sep;58(15):5097–108.

43. Mullins WW. Theory of Thermal Grooving. J Appl Phys. 1957 Mar 1;28(3):333–9.

44. Chemistry LibreTexts [Internet]. 2013 [cited 2023 Nov 28]. Propagation of Error. Available from: https://chem.libretexts.org/Bookshelves/Analytical_Chemistry/Supplemental_Modules_(Analytical_Chemistry)/Quantifying_Nature/Significant_Digits/Propagation_of_Error

45. Johnson JR. Phase Diagrams for Ceramists. Nucl Sci Eng. 1965 Jun;22(2):275–6.

46. Liu Q, Bhattacharya S, Helmick L, Donegan SP, Rollett AD, Rohrer GS, et al. Crystallography of Interfaces and Grain Size Distributions in Sr -Doped LaMnO 3. Blendell J, editor. J Am Ceram Soc. 2014 Aug;97(8):2623–30.

47. Xu Z, Hefferan CM, Li SF, Lind J, Suter RM, Abdeljawad F, et al. Energy dissipation by grain boundary replacement during grain growth. Scr Mater. 2023 Jun;230:115405.

48. Xu Z, Shen YF, Naghibzadeh SK, Peng X, Muralikrishnan V, Maddali S, et al. Grain boundary migration in polycrystalline α-Fe. Acta Mater. 2024 Jan;264:119541.

49. Rollett AD, Srolovitz DJ, Anderson MP. Simulation and theory of abnormal grain growth—anisotropic grain boundary energies and mobilities. Acta Metall. 1989 Apr;37(4):1227–40.

50. Hwang NM. Simulation of the effect of anisotropic grain boundary mobility and energy on abnormal grain growth. J Mater Sci. 1998;33(23):5625–9.

51. Bojarski SA, Harmer MP, Rohrer GS. Influence of grain boundary energy on the nucleation of complexion transitions. Scr Mater. 2014 Oct;88:1–4.

52. Bäurer M, Shih SJ, Bishop C, Harmer MP, Cockayne D, Hoffmann MJ. Abnormal grain growth in undoped strontium and barium titanate. Acta Mater. 2010 Jan;58(1):290–300.

53. Sternlicht H, Rheinheimer W, Hoffmann MJ, Kaplan WD. The mechanism of grain boundary motion in SrTiO3. J Mater Sci. 2016 Jan;51(1):467–75.

54. Rheinheimer W, Schoof E, Selzer M, Nestler B, Hoffmann MJ. Non-Arrhenius grain growth in strontium titanate: Quantification of bimodal grain growth. Acta Mater. 2019 Aug;174:105–15.

55. Ruddlesden SN, Popper P. The compound Sr $_3$ Ti $_2$ O $_7$ and its structure. Acta Crystallogr. 1958 Jan 1;11(1):54–5.

56. Šturm S, Rečnik A, Scheu C, Čeh M. Formation of Ruddlesden–Popper faults and polytype phases in SrO-doped SrTiO $_3$. J Mater Res. 2000 Oct;15(10):2131–9.

57. Amaral L, Fernandes M, Reaney IM, Harmer MP, Senos AMR, Vilarinho PM. Grain Growth Anomaly and Dielectric Response in Ti-rich Strontium Titanate Ceramics. J Phys Chem C. 2013 Nov 27;117(47):24787–95.

58. Amaral L, Senos AMR, Vilarinho PM. Sintering kinetic studies in nonstoichiometric strontium titanate ceramics. Mater Res Bull. 2009 Feb;44(2):263–70.